Computational Design of Alloy Nanostructures for Optical Sensing of Hydrogen

Downloaded from: https://research.chalmers.se, 2026-04-03 04:51 UTC

Citation for the original published paper (version of record):
Ekborg-Tanner, P., Rahm, M., Rosendal, V. et al (2022). Computational Design of Alloy Nanostructures for Optical Sensing of Hydrogen. ACS Applied Nano Materials, 5(8): 10225-10236. http://dx.doi.org/10.1021/acsanm.2c01189

N.B. When citing this work, cite the original published paper.

research.chalmers.se offers the possibility of retrieving research publications produced at Chalmers University of Technology. It covers all kind of research output: articles, dissertations, conference papers, reports etc. since 2004. research.chalmers.se is administrated and maintained by Chalmers Library

(article starts on next page)

ACS APPLIED NANO MATERIALS

www.acsanm.org Article

Computational Design of Alloy Nanostructures for Optical Sensing of Hydrogen

Pernilla Ekborg-Tanner, J. Magnus Rahm, Victor Rosendal, Maria Bancerek, Tuomas P. Rossi, Tomasz J. Antosiewicz, and Paul Erhart*

Cite This: https://doi.org/10.1021/acsanm.2c01189 Read Online

ACCESS | Metrics & More | Article Recommendations | Supporting Information

ABSTRACT: Pd nanoalloys show great potential as hysteresis-free, reliable hydrogen sensors. Here, a multiscale modeling approach is employed to determine optimal conditions for optical hydrogen sensing using the Pd−Au−H system. Changes in hydrogen pressure translate to changes in hydrogen content and eventually the optical spectrum. At the single particle level, the shift of the plasmon peak position with hydrogen concentration (i.e., the "optical" sensitivity) is approximately constant at 180 nm/c_H for nanodisk diameters of $\gtrsim$100 nm. For smaller particles, the optical sensitivity is negative and increases with decreasing diameter, due to the emergence of a second peak originating from coupling between a localized surface plasmon and interband transitions. In addition to tracking peak position, the onset of extinction as well as extinction at fixed wavelengths is considered. We carefully compare the simulation results with experimental data and assess the potential sources for discrepancies. Invariably, the results suggest that there is an upper bound for the optical sensitivity that cannot be overcome by engineering composition and/or geometry. While the alloy composition has a limited impact on optical sensitivity, it can strongly affect H uptake and consequently the "thermodynamic" sensitivity and the detection limit. Here, it is shown how the latter can be improved by compositional engineering and even substantially enhanced via the formation of an ordered phase that can be synthesized at higher hydrogen partial pressures.

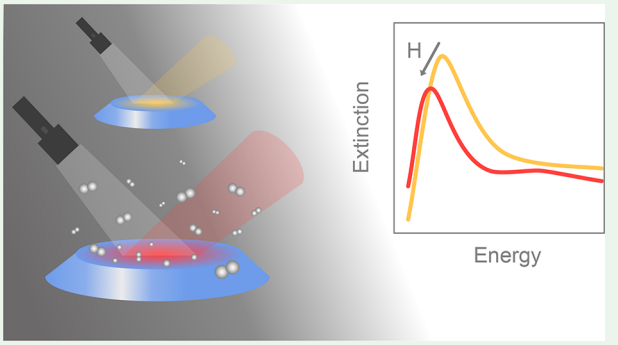

KEYWORDS: *hydrogen sensing, nanoplasmonics, localized surface plasmon resonance, nanoparticles, palladium alloys, dielectric function*

INTRODUCTION

One of the main challenges of the hydrogen economy, a future energy system where fossil fuels have been replaced with hydrogen-based fuels, is the flammability of hydrogen gas under ambient conditions.[1] As a result, hydrogen sensing continues to be a very active research field with the goal of providing fast, reliable, and long-term stable hydrogen sensors that can prevent major accidents. Several different sensing platforms have been proposed, typically based on the change in optical[2−12] or electrical[13−15] properties of a material during hydrogen absorption. Many of these devices are based on palladium (Pd), which forms a hydride phase upon exposure to a hydrogen-rich atmosphere. The electronic properties of the hydrogenated system differ from the hydrogen-free one, leading to a shift in the optical response as well as a change in resistivity, which can be measured and related to the hydrogen pressure in the surrounding environment. In this work, we focus on optical sensors based on the localized surface plasmon resonance (LSPR) of Pd−Au-based nanoalloys[2,3,6,9] and show how they can be optimized via geometry and alloy composition.

A significant shortcoming of hydrogen sensors based on pure Pd nanoparticles (NPs) is that they undergo a first-order phase transition upon hydrogenation, from the hydrogen-poor α to the hydrogen-rich β-phase, which leads to a nonlinear, discontinuous response to hydrogen pressure. The phase transition is further associated with significant hysteresis,[16] which ultimately makes the response of the sensor dependent on its history. It has been shown that these disadvantages can be overcome by alloying.[17,18] Specifically, the introduction of about 20% of gold (Au) suppresses the phase transition, making the response of the sensor a linear function of hydrogen pressure.[6,17,19−21] To optimize these systems for hydrogen sensing, important questions remain: in what proportions should we mix the two alloyants, what shapes should the NPs have, and what features of the optical response should the sensing mechanism be based on? Historically, similar questions have been addressed by trial-and-error experiments. While that is a viable approach, the additional

Received: March 17, 2022
Accepted: July 8, 2022

See https://pubs.acs.org/sharingguidelines for options on how to legitimately share published articles.

ACS Publications © XXXX The Authors. Published by American Chemical Society

Scheme 1. Methodological Overview[a]

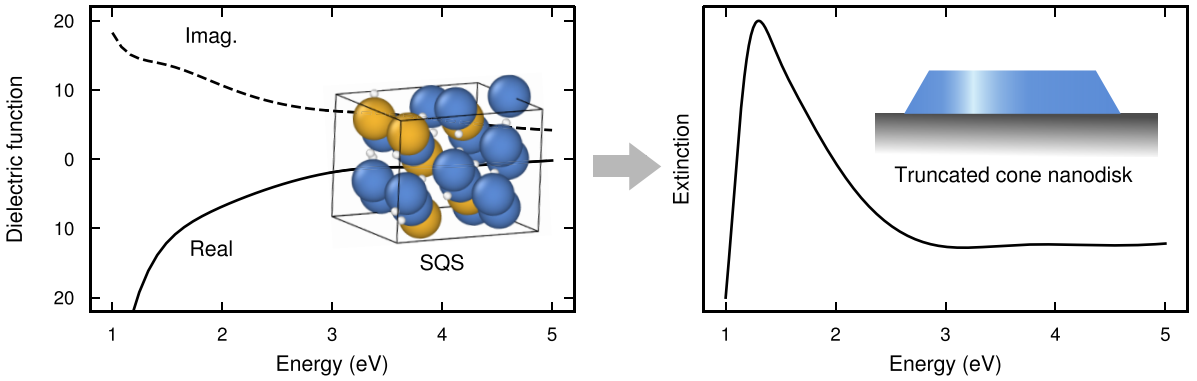

[a]First, the dielectric functions are calculated for special quasi-random structures (SQSs) in bulk for a wide range of alloy and H concentrations using linear-response time-dependent density-functional theory (left). Second, the corresponding extinction spectra are calculated for truncated cone nanodisks of varying dimensions (right) using electrodynamic simulations, which are in turn used to analyze the optical sensitivity.

degrees of freedom introduced by mixing two or more components and the large space of available geometries make it extraordinarily cumbersome to experimentally test all combinations of potential interest. In this context, a multiscale modeling approach that resolves the variation in electronic properties with composition and translates this variation to the optical properties of NPs of different sizes and shapes is therefore invaluable.

The dielectric function (DF) links electronic and optical properties, as well as atomic and continuum scales. We have recently calculated the DFs of 10 binary alloys in their full composition range and demonstrated that electrodynamic simulations based on these DFs provide accurate predictions of the optical response of alloy nanoparticles.[22] Earlier studies of pure Pd have shown, in principle, how one can combine electronic structure calculations and electrodynamic simulations to enable multiscale modeling of the optical response during hydrogenation.[23,24] They were, however, limited in the representation of chemical order (due to very small structure models) and also did not consider Pd-alloys. Here, we build on and extend the underlying approach to calculate the DFs of Pd−Au alloys with up to 46% Au and in the full range from no hydrogen to full hydrogen loading. The DFs are then converted to a Lorentzian representation and used in electrodynamic simulations to predict the extinction spectra of Pd−Au nanodisks (Scheme 1). Finally, the optical sensitivity of hydrogen sensors based on Pd−Au NPs is derived from the changes in their extinction spectra. To obtain the actual sensitivity one must also include a thermodynamic factor that accounts for the solubility of hydrogen in the material, which here is taken into account using a thermodynamic model developed previously.[25] This multiscale approach, which extends from first-principles calculations on the atomic scale to electrodynamic simulations on the macroscale, is not limited to hydrogenated Pd−Au nanoparticles but can in principle be applied to the optical response of any material.

An important aspect in this context is atomic scale ordering, which has the potential to significantly alter the DF and, in turn, the optical response.[22] This situation requires careful consideration when calculating DFs from first-principles and applying them to the prediction of the optical response of nanoalloys. In thermodynamic equilibrium and in the absence of hydrogen, bulk Pd−Au is expected to form an alloy without long-range order and at most a low degree of short-range order.[25,26] Furthermore, since in many studies the nanoalloys are annealed at high temperatures,[6,17,21] it is safe to assume that the chemical distribution of the alloyants is close to random. To represent this situation in our calculations, we use special quasi-random structures (SQSs),[27] which are constructed to reproduce the (lack of) short-range order in a truly random alloy using unit cell sizes that are small enough for efficient calculations (in our case 24 Au/Pd atoms and 0−24 H atoms). As discussed before,[25,26,28] exposure to hydrogen can, however, impact thermodynamics and ordering. As the nanoalloys are typically only exposed to hydrogen at high temperatures during fabrication and for short periods of time during operation, it is reasonable to assume that this effect is negligible for the samples produced in, for example, refs 6, 17, and 21. It is, however, known from both experimental and theoretical evidence that an ordered, intermetallic phase can emerge for compositions around 25% Au after annealing at high hydrogen pressures and moderate temperatures.[25,26] As we will show in this work, the presence of this phase could potentially improve the sensing ability at low hydrogen pressures radically.

RESULTS AND DISCUSSION

Electronic Structure and Dielectric Functions. We begin by examining the DFs as calculated with linear-response time-dependent density-functional theory (Figure 1a,b; see Figure S1 and Figure S2 for the real and imaginary parts at more compositions and in a wider energy range). A few trends are apparent.

In the case of Pd−H, addition of H leads to the emergence of two peaks in the imaginary part of the DF that at 100% H loading are located around 1.5 eV and at approximately 3.0−3.5 eV (Figure 1a). Comparison with the density of states (DOS) indicates that these two features are related to two pronounced peaks in the d band (Figure 1c; see Figure S3 for the DOS at more compositions). In fact in this case, the DOS in its entirety is almost unaffected by H addition, save for a rigid shift of the energy scale. This is a result of the localized character of the H states, which do not hybridize with each other. Addition of H also reduces the magnitude of the real part of the DF in the visible range, as has been previously observed in both experiment[29,30] and computations[24] (Figure S4). Generally speaking, such a trend is expected to imply a

https://doi.org/10.1021/acsanm.2c01189
ACS Appl. Nano Mater. XXXX, XXX, XXX−XXX

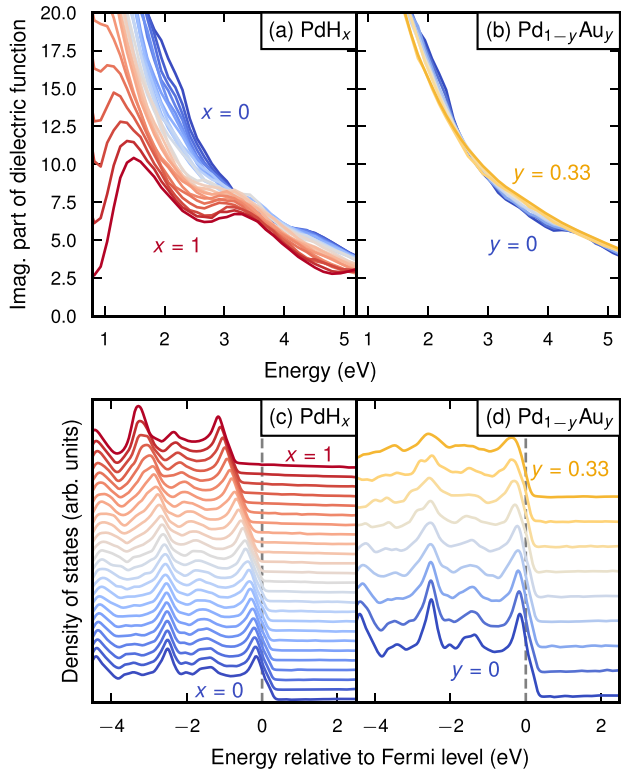

Figure 1. Variation of the imaginary part of the dielectric function as a function of photon energy for (a) PdH_x without Au and (b) $Pd_{1-y}Au_y$ in the absence of H, as calculated in this work. The dielectric function is closely related to the density of states (c, d). Energies have been shifted such that the Fermi level is always at 0 eV.

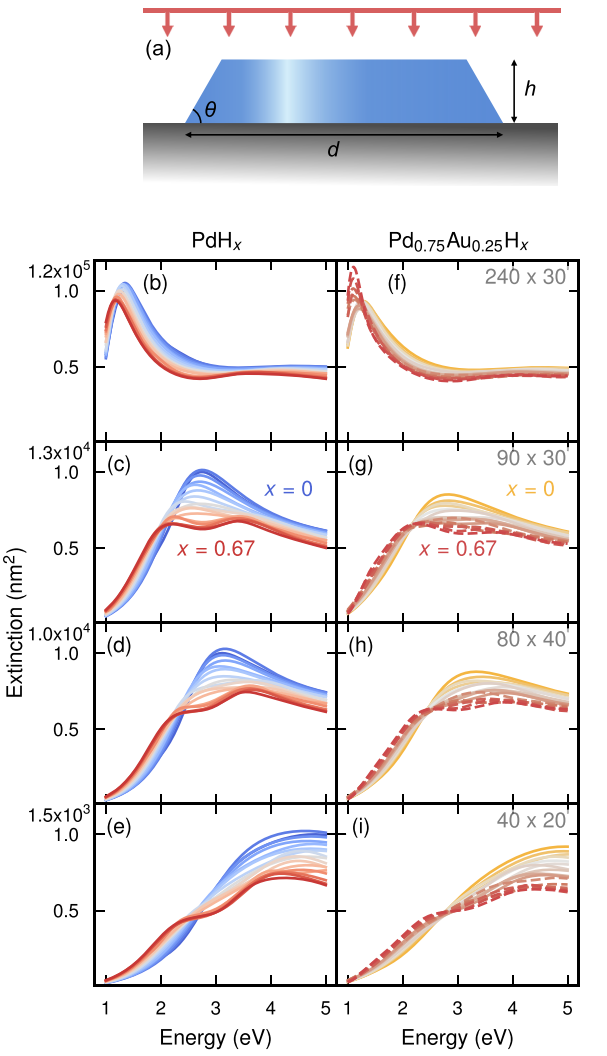

Figure 2. Optical response of truncated cone nanodisks of varying height h and diameter d and fixed cone angle $\theta = 60°$ (a). Here, we show the extinction spectra for disk geometries ($d \times h$ in nm): 240 × 30 (b, f), 90 × 30 (c, g), 80 × 40 (d, h), and 40 × 20 (e, i) with 0% Au (b–e) and 25% Au (f–i) at H concentrations 0–67%. The dashed lines correspond to H concentrations $c_H > 0.67 - c_{Au}$, which are excluded in the calculations of the optical sensitivity $\tilde{S}$.

redshift of the plasmon peak, as the Fröhlich condition for LSPR emergence is satisfied at lower energies.

Upon addition of Au to Pd, there is almost no change in the imaginary part of the DF in the composition range considered here (Figure 1b). In the DOS, on the other hand, a notable smoothing occurs as a result of hybridization between the d states of Pd and Au (Figure 1d).[31] Therefore, when H is added to Pd–Au, the two peaks that were apparent in the DF of Pd–H are largely smoothed out due to alloy disorder (Figure S2).

Optical Response. After fitting the DFs to a Lorentzian representation (as described in Supplementary Note 1) we carry out electrodynamic simulations of the optical response of truncated cone nanodisks (Figure 2a), characterized by their height h (20–40 nm) and aspect ratio (AR) (2–12) or diameter d = AR × h on a silica substrate, mimicking a single nanodisk fabricated by the hole-mask colloidal lithography method.[32] The exact shape of the nanodisk is, however, not of great importance (see Figure S5 for a comparison between slightly differently shaped nanodisks).

Pd–H Nanodisks. We begin by studying the optical response of the Pd–H system based on the calculated extinction. In Figure 2b–e the extinction spectra for four specific geometries are shown (see Figure S6 for separate scattering and absorption spectra). These are selected since they represent different characteristics of the studied spectra (see Figure S7 for the full range of geometries). The shape of the extinction spectra varies with geometry and H content, but at least one peak can be identified for all systems. Most geometries considered have extinction spectra similar to Figure 2b with a well-defined, relatively sharp peak that shifts to the red with increasing H content. For smaller nanodisks, however, the features are broader and we can identify two distinct peaks at H concentrations above 50% (Figure 2c–e). The second peak emerges with increasing H content and decreasing height and diameter and becomes the dominant feature in the high H loading limit for the smallest particles considered here.

The high-energy feature is in fact present for all geometries in the high H limit, but for larger nanostructures (such as the one in Figure 2b) this feature is less noticeable due to the larger amplitude of the low-energy peak. Of these two peaks, the high-energy one is roughly constant in energy (and amplitude; see Figure S8) while the low-energy peak shifts when the aspect ratio is varied. To illustrate this behavior, we compare the cases of 0% and 100% H in Pd, which allows one to identify the key features in the DFs more easily due to the lack of disorder on the H sublattice. For 0% H in Pd, we observe one peak that shifts from 1 eV for large nanodisks to 5 eV for small nanodisks (Figure 3a), in agreement with the expected size dependence of a LSPR. For 100% H in Pd, on

https://doi.org/10.1021/acsanm.2c01189
ACS Appl. Nano Mater. XXXX, XXX, XXX–XXX

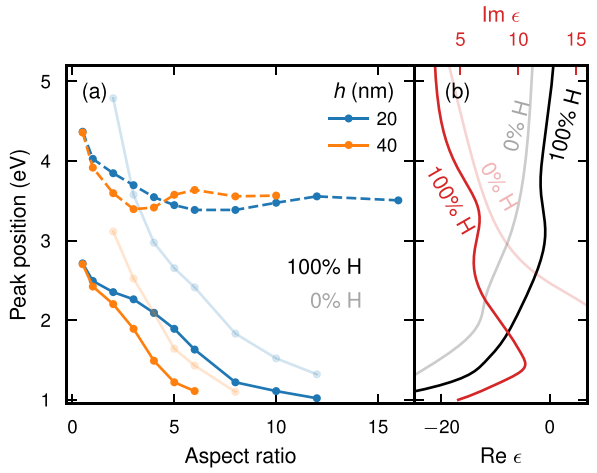

Figure 3. Peak position of the two peaks in the extinction spectra for PdH (opaque lines) and Pd (transparent lines) as a function of aspect ratio for two disk heights h (a) and the corresponding dielectric functions (b). PdH displays two features, one low-energy peak (solid line) which shifts with aspect ratio and one high-energy peak (dashed lines) which only shifts for small aspect ratios, indicating avoided-crossing behavior due to coupling between the peaks. The high-energy peak can be traced to the feature at 3.5 eV in the dielectric function (b) for 100% H (opaque line). This feature is not present for 0% H (transparent line), and as a result, the LSPR peak can shift over a much wider energy interval (transparent lines in b). Note that (b) shows the fitted Lorentzian representation of the dielectric functions.

the other hand, we observe two peaks (see the corresponding extinction spectra and field enhancement in Figure S9). For nanodisks with larger ARs, the peaks are separated in energy and the low-energy peak increases in energy with decreasing AR (as expected for a LSPR) while the high-energy peak remains at about 3.5 eV (Figure 3a). The lack of size dependence for the high-energy peak indicates that it is caused by a bulk phenomenon, such as a spectrally localized interband transition.[33,34] When a LSPR peak moves closer to an interband transition, they can couple and exhibit avoided crossing.[33,34] This is precisely the behavior we observe for small ARs when the shift of the low-energy feature is restricted (compared to the 0% H case) and the high-energy peak starts to increase in energy. The presumed interband transition can be related to the previously discussed feature in the DF close to 3.5 eV (Figure 3b and section Electronic Structure and Dielectric Functions). For 0% H in Pd there is no such feature, and as a result, there is no avoided crossing for 0% H and the LSPR peak can shift over the entire energy interval without interference.

Pd−Au−H Nanodisks. We now turn to the impact of Au on the extinction spectra. For comparison with previous experimental studies,[6,21] we focus on 25% Au which provides a trade-off between suppressing the hysteresis and avoiding the decrease in H absorption with increased Au concentration (Figure S10). The introduction of 25% Au has a relatively small effect on the optical response (Figure 2). Some changes in the extinction spectra can, however, be identified. For the most part, introducing Au leads to a broader extinction spectrum with slightly lower peak amplitude and a weaker tendency for peak splitting (Figure 2g−i). This is consistent with the observation that the DOSs and the DFs are typically smoothed by adding Au to Pd; features are blurred out by the chemical disorder. In the case of large AR and high H content, however, the LSPR peak becomes sharper and more intense with increasing Au content (Figure 2f). This sharpening is a consequence of the increased distance between d band and Fermi level in systems with high Au and/or H content (Figure 1c), which reduces the ability of the d electrons to screen the LSPR at low energies. Peak splitting occurs in the high H limit for Pd−Au nanodisks as well, but the evolution of the high-

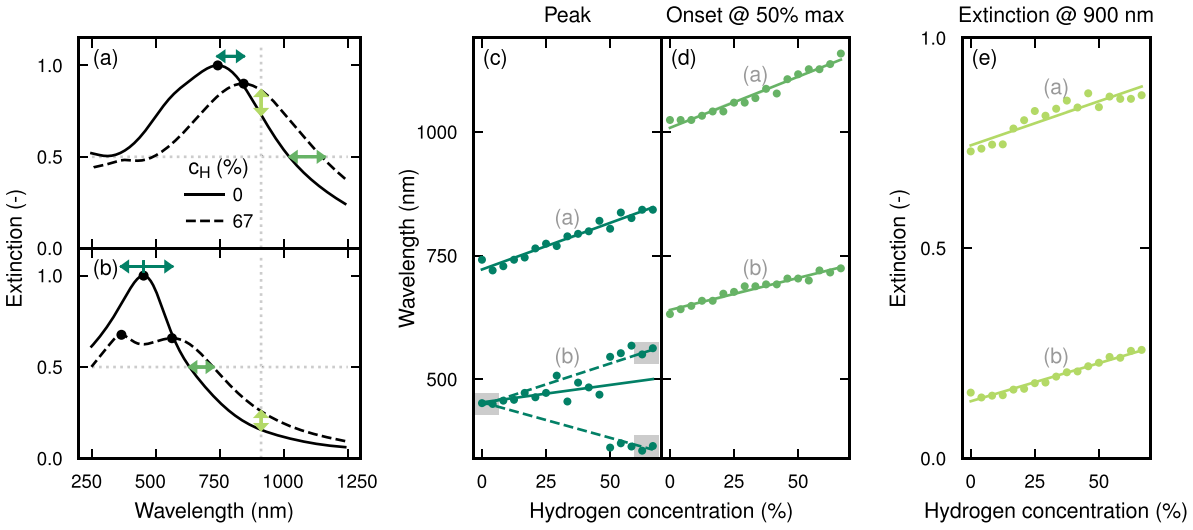

Figure 4. For a given set of extinction spectra, such as the spectra (a) without or (b) with pronounced peak splitting, one can define the optical sensitivity $\tilde{S}$ based on several different shifts with H content (illustrated here for Pd−H). First, the peak position (black dots in (a) and (b)) generally shifts linearly with H concentration (c). For the case of pronounced double peaks, we study the peak shift both excluding data points with double peaks (solid lines in (c)) and with double peaks (dashed lines in (c)). In the latter case, only the data points corresponding to the two lowest and two highest H concentrations (indicated by the shaded regions) contribute to the fit. Second, the wavelength at a certain onset amplitude (50% of the peak extinction at 0% H here) has a similar linear increase with increased H content (d). Third, the extinction at a particular wavelength (900 nm here) also shows an almost linear dependence on the H concentration (e), although the trend deviates slightly from linearity close to the peak(s). In all these cases, the optical sensitivity $\tilde{S}$ can be defined as the slope of the linear trend(s).

https://doi.org/10.1021/acsanm.2c01189
ACS Appl. Nano Mater. XXXX, XXX, XXX−XXX

energy peak with size or H content is considerably less regular compared to the case of Pd. This is related to the corresponding somewhat irregular evolution of the alloy DFs which is caused by the imperfect representation of the chemical order due to limited system size.

Optical Sensitivity Optimization. In general, sensitivity is defined as the ratio between the output signal and the underlying external stimulus. In *optical* sensing it is common to follow the variation of one or more characteristic descriptors of the optical spectrum as measures of the output signal, which in the present case of plasmonic sensing are related to the behavior of the plasmon peak, e.g., its amplitude, width or position, or the surrounding spectral region. In the specific case of hydrogen sensing the external stimulus is the presence of H_2 in the surrounding environment as expressed by its partial pressure p_{H_2}. More formally the sensitivity of such a sensor, using here the position of the plasmon peak λ_{max} for illustration, can be written as

$$S = \frac{d\lambda_{max}}{dp_{H_2}} \tag{1}$$

Earlier measurements for this material system[2,3,6,9] have, however, commonly considered the change in the absorption maximum λ_{max} with the hydrogen concentration in the material c_H,

$$\tilde{S} = \frac{d\lambda_{max}}{dc_H} \tag{2}$$

The two measures are related to each other via

$$S = \frac{d\lambda_{max}}{dc_H} \times \frac{dc_H}{dp_{H_2}} = \tilde{S}S_{sol} \tag{3}$$

where the subscript emphasizes that S_{sol} directly depends on the solubility of hydrogen as a function of its partial pressure.

In the present section, we will focus entirely on $\tilde{S}$, for brevity referred to as the optical sensitivity. We will return to the role of S_{sol} in the section Thermodynamic Optimization.

In the following, we study three specific measures for the optical sensitivity $\tilde{S}$ based on the shift in peak position (*peak shift*), wavelength at a fixed extinction amplitude onset (*onset shift*), and extinction at a certain wavelength (*extinction shift*), respectively (Figure 4), with respect to the absorbed H concentration to determine the limits of optical sensitivity optimization through engineering of composition and/or geometry.

In the case of Pd−H, the H concentration range that is relevant under common thermodynamic conditions is rather wide, while it is more narrow for Pd−Au−H. As a consequence, we have chosen to restrict the maximum H concentration considered to $c_H < 0.67 - c_{Au}$ when calculating the sensitivities, which is sufficient for hydrogen pressures up to 1 bar (Figure S10). The exact limit is not of great importance since the studied shifts are generally linear with H concentration for hydrogen pressures of $\lesssim$1 bar.

Peak Shift. In ref 6, the (optical) sensitivity was defined as the ratio of the peak shift to the change in H concentration. For a specific geometry, the peak position is generally an approximately linear function of the H concentration (Figure 4c), and the sensitivity can be obtained as the slope of the corresponding linear fit. This is straightforward for the larger nanostructures considered (i.e., disks well-represented by Figure 4a) that feature one dominant peak for all H concentrations.[35] For the smaller nanodisks considered here, peak splitting, however, comes into play which complicates the determination of the optical sensitivity. In systems with significant peak splitting (e.g., see Figure 4b), we therefore consider two different peak shift sensitivities. First, we fit the peak shift as a function of H concentration after excluding all H concentrations with peak splitting (solid line in Figure 4c). Note that with this approach, cases with pronounced peak splitting typically result in a large fitting error since the data points are characterized by large scatter (see Figure S13 for the fitting errors). Second, we fit the peak shift based on only the first two data points (low H limit) and the last two data points (high H limit) for either peak separately (dashed lines in Figure 4c), resulting in two sets of sensitivities, typically with opposite signs. The latter approach is suitable for pure Pd and low Au content since the phase transition introduces a jump from low to high hydrogen content (Figure S10). For high Au content ($\gtrsim$10%), peak splitting is in practice not an issue since the hydrogen content is below 50% at relevant pressures (Figure S10).

In Figure 5a, we display the obtained peak shift sensitivity for all considered systems as a function of the disk diameter. Clearly, the size dependence of the sensitivity can be divided into two regimes. Nanodisks with diameter of $\gtrsim$100 nm have a roughly constant sensitivity around 180 nm/(H/(Au + Pd)), which to a large degree is independent of disk height and alloy composition. Smaller nanodisks, however, follow a linearly decreasing trend with increasing diameter. The double peak sensitivities (semicircles in Figure 5a) follow the same trends and introduce an overlap between the two regimes. The trend for small nanodisks can be explained by the peak splitting. When the high-energy peak at 67% H ($\lambda_{H_{max}}$) dominates over the corresponding low-energy peak, the sensitivity is determined by the shift between the 0% H peak (λ_0) and the former. In a simplified picture, λ_0 shifts to lower wavelengths with decreasing diameter while $\lambda_{H_{max}}$ is constant. This means that, as the diameter is decreased, the sensitivity will shift from strongly negative to positive, crossing zero when λ_0 and $\lambda_{H_{max}}$ align.

The optical sensitivity trends are largely unaffected by the introduction of up to 25% Au (Figure 5a). This is somewhat surprising since for Pd the sensitivity is almost entirely determined by peak splitting and for Pd−Au the peak splitting is less distinct and often not relevant due to the H concentration threshold. Clearly, the peak shift sensitivity is not very sensitive to the details in the shape of the extinction spectra.

In Figure 5a, we include experimental results from ref 6, where the authors find a linear increase in the (optical) sensitivity as a function of the peak position at 0% H.[36] While the experimental trend can be interpreted to reach a plateau for peak positions at 0% H of $\gtrsim$600 nm, there is still an apparently large discrepancy with our findings. Note, however, that the experimental results were obtained for nanodisk *arrays* and the measurements thus correspond to an average over a large *ensemble* of particles. Notably, the measured (optical) sensitivity is very close to zero right at the discontinuity between the two sensitivity regimes, where peak-splitting is most pronounced. This could suggest that the experimentally measured linear increase in sensitivity is due to a superposition

https://doi.org/10.1021/acsanm.2c01189
ACS Appl. Nano Mater. XXXX, XXX, XXX−XXX

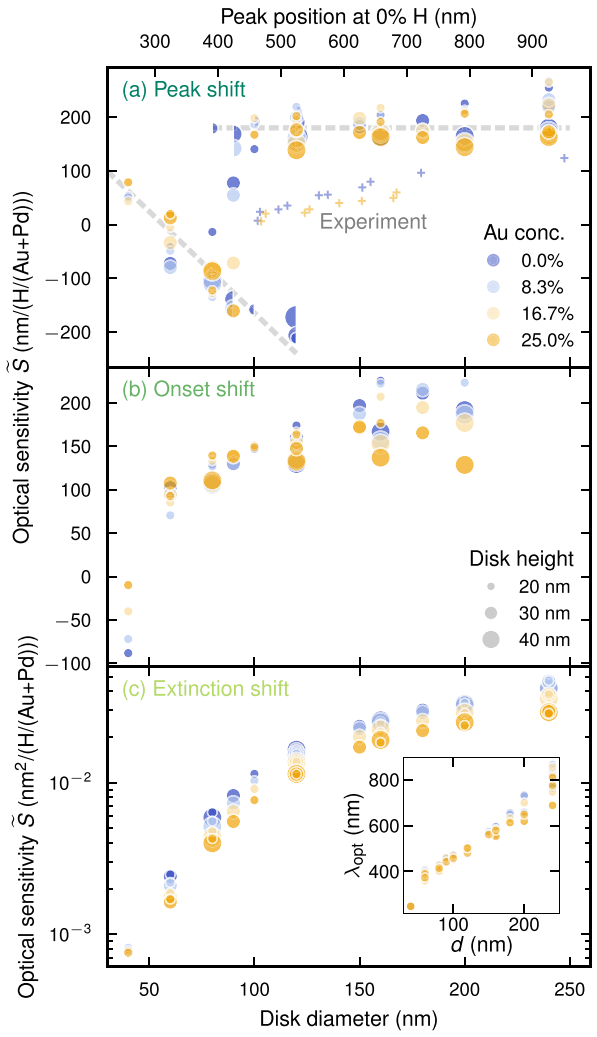

Figure 5. Optical sensitivity of Pd−Au nanodisks with varying Au content as a function of the disk diameter, in terms of (a) peak shift, (b) onset shift, and (c) extinction shift at λ_{opt} per unit H uptake. In (a), semicircles correspond to the sensitivity when peak-splitting is taken into account (as explained in Figure 4) and plus signs show experimental data from ref 6. Note that the experimental sensitivity is rescaled from nm/(H/Pd) to nm/(H/(Au + Pd)) and the disk diameter is approximated by the linear relation in Figure S12b. The corresponding peak position at 0% H is indicated by the upper *x*-axis scale, calculated from the diameter and the linear relation in Figure S12b. In (c), the inset shows the wavelength where the optimal sensitivity was found for each system.

of nanoparticle shapes and sizes that fall on either side of the discontinuity between the sensitivity regimes, and as the fraction of particles which display peak splitting decreases, the sensitivity increase. We address this aspect in detail in the section Uncertainty Analysis but find that size distribution and array effects on their own are insufficient to explain this effect.

Onset Shift. Another way of defining the optical sensitivity, which circumvents keeping track of peaks, is to monitor the wavelength at the onset of a fixed target extinction amplitude. Here, we define the target amplitude as 50% of the peak amplitude at 0% H (Figure 4a,b) and track the corresponding wavelength (to the right of the peak in wavelength) as a function of the H concentration (Figure 4d).[37]

The onset shift generally follows a linear trend with respect to H concentration, the slope of which can be defined as the sensitivity (Figure 5b). For almost all considered geometries, such as the ones in Figure 4a,b, we obtain a positive sensitivity that increases slightly with increasing diameter. For very small nanostructures, however, the low energy peak at high H content falls below the onset amplitude (Figure 2e,i), which reverses the direction of the onset shift and results in a small or negative sensitivity. In principle, this issue could be resolved by decreasing the onset amplitude value below 50%. That would, however, push the amplitude onset for the largest nanodisks beyond the low energy (high wavelength) limit.

The introduction of Au slightly reduces the slope of the sensitivity trend such that the sensitivity of the largest nanodisks decreases with increased Au content.

Extinction Shift at a Certain Wavelength. A third possible optical sensitivity definition is based on the shift in extinction amplitude at a certain wavelength (Figure 4a,b,e). This definition is of particular interest for real devices since it does not require measuring the spectrum over the entire spectral range but only at a single wavelength. In Figure S14, we display extinction spectra at increasing H content in terms of extinction at selected energies (Figure S14a−d) and the corresponding slope of linear fits (Figure S14e−h).

The slope changes significantly with energy from a positive value to the left of the peak to a negative value to the right of the peak. This means that the choice of wavelength is crucial for maximizing the optical signal. For each system we define the wavelength for which the largest slope (in absolute value) is obtained as λ_{opt}. The extinction shift sensitivity is defined as the absolute value of the slope at λ_{opt} in units corresponding to extinction cross section (Figure 5c). The sensitivity increases with disk diameter, decreases slightly with Au content, and in the size range considered is independent of disk height. It should be noted that, in contrast to peak and onset shift, the extinction shift is proportional to the amplitude of the optical response of an individual nanodisk. As a result, the sensitivity increase is to a large degree caused by the increase in extinction cross section with size (Figure 2). In a real device, the number of nanodisks per area can be increased for smaller particles which means that for some purposes, it might be more relevant to compare the extinction-shift sensitivity scaled with nanodisk area.

Uncertainty Analysis. As previously noted, there is a discrepancy between our results and an earlier experimental study[6] for the peak shift sensitivity. Such differences between experiment and simulations are not unexpected given the many uncertainties involved, which exist both at the level of the electrodynamic simulations of the optical response and at the level of the electronic structure calculations of the DFs. Here, we investigate the impact of the sources of discrepancy that we judge to be the most important.

Let us first consider the effect of particle size distribution and array effects on the optical spectrum, which enter at the level of the electrodynamic simulations. In contrast to the single particles simulated in this work, the experimental samples consist of many irregularly shaped nanoparticles with a significant size distribution.[6] These particles are furthermore randomly distributed on a substrate, leading to array effects that are known to influence the optical spectrum.[39] We observe that the naive approach of weighting extinction spectra according to some size distribution does not significantly alter the extinction (Figure S15). To better mimic the experimental situation, we therefore performed additional simulations of random arrays of nanoparticles (using the T-

https://doi.org/10.1021/acsanm.2c01189
ACS Appl. Nano Mater. XXXX, XXX, XXX−XXX

matrix method as described in the section T-Matrix Simulations). While the array effects (but to a lesser extent the size distribution) do change the position and sharpness of the peak (Figure S16; also see ref 40), the sensitivity trends remain similar to the single particle results (Figure 6).

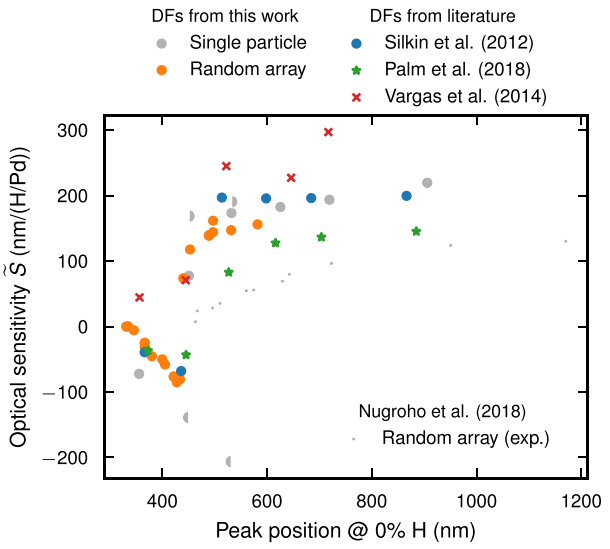

Figure 6. Optical peak shift sensitivity $\tilde{S}$ for Pd nanodisks with 30 nm diameter calculated using different computational setups and DFs. The data from Figure 5a are included in gray. The sensitivities for explicit and effective random arrays (orange), with and without size distribution, follow closely the previously discussed trends for single particles (large gray (semi)circles). The sensitivities obtained using DFs from Silkin et al.,[24] Palm et al.,[29] and Vargas et al.[30] show a large spread. Note that, except for the data in gray, the sensitivities here are calculated based on only the peaks at 0% and ~67% H [38] in order to reduce the computational effort.

A further source of uncertainty is the DFs, which in the present work are obtained from electronic structure calculations. The calculated DF depends on the underlying electronic structure method, in the present case primarily the exchange−correlation functional, but also on the treatment of scattering, especially due to defects (e.g., including surfaces, grain boundaries, and dislocations) and chemical disorder in the case of alloys. With regard to the description of the electronic band structure, the present approach yields results that are in very good agreement with recent highly accurate many-body theory calculations.[41] We therefore focus our attention on the possible effect of scattering mechanisms. In Figure 6, we compare the optical sensitivity calculated using three sets of DFs from the literature; two experimentally measured ones (Vargas et al.[30] and Palm et al.[29]) and one calculated using an approach similar to ours (Silkin et al.[24]). Although the DFs are in semiquantitative agreement over the energy range considered (Figure S4), small differences clearly can have a large effect on the resulting sensitivity. Note in particular the large span of sensitivities resulting from the *experimentally measured* sets of DFs, while the calculated set of DFs yield sensitivities very similar to our original findings. Real samples are typically subject to defect scattering which leads to a broadening of the Drude peak. This effect is very difficult to include rigorously at the ab initio level and is furthermore sample-dependent, which could explain the large difference between the two experimentally measured sets of DFs. To illustrate this aspect further, it is instructive to consider the case of the noble metals, for which the d-band feature in the DFs is clearly separated from the Drude peak and thus allows one to observe the effect of defect scattering more directly. This reveals the large variation in the width of the Drude peak caused by differences in sample preparation and the resulting defect density (e.g., see Figure S1a−c of ref 22). In the case of Pd alloys and hydrides the d-band overlaps with the Fermi level, which leads to a very broad response in the low-energy region and the impact of (defect) scattering cannot be clearly separated. This makes it difficult to include this contribution systematically at the level of the DFs and eventually assess its impact on the optical response.

Regardless of which set of DFs is used, a large shift in sensitivity appears when the peak position at 0% H is at approximately 450 nm, which is also where the experimentally measured sensitivity goes to zero, in line with the discontinuity between the two sensitivity regimes previously discussed. This indicates that it is in fact the interband transition at high H content that is responsible for large changes of the sensitivity. We verified this argument by explicitly removing the associated Lorentzian from the DF, which results in a sensitivity that remains at a high, positive value even as the peak position at 0% moves below 450 nm (Figure S17).

Lastly, we observe that by introducing artificial Lorentzian broadening in the simulated extinction spectra, a linear increase in the sensitivity similar to the experimental results can be obtained (Figure S18), although quite extreme levels of broadening are necessary. We conclude that it is in general very difficult to account quantitatively for the sample-specific broadening channels.

Thermodynamic Optimization. Above, in agreement with earlier experimental studies, we have seen that the alloy composition is not crucial for the *optical* sensitivity $\tilde{S}$. It is, however, crucial for the *thermodynamic* sensitivity S_{sol} and hence impacts the actual sensitivity S see eq 3. In this section, we therefore analyze the dependence of the *thermodynamic* sensitivity S_{sol} on alloy composition and then translate the results to a detection limit in terms of the hydrogen pressure. In this context, we also show that the highest sensitivities are obtained for the ordered $L1_2$-Pd_3Au phase.

Thermodynamic Sensitivity. For the following analysis, we limit us to a temperature of 300 K and use the relationships between partial pressure of H_2, Au concentration, and H concentration established in ref 25 by means of alloy cluster expansions, Monte Carlo simulations, and experimental data (Figure 7a and Figure S10). Using these data, one can compute the (differential) thermodynamic sensitivity (also see eq 3),

$$S_{sol} = \frac{dc_H}{dp_{H_2}} \tag{4}$$

In practice one is, however, more often interested in the change relative to a reference pressure, representing a situation in which one aims to probe a sudden increase in hydrogen pressure relative to a low background level. Here, we therefore consider the thermodynamic sensitivity defined as

$$\tilde{S}_{sol} = \frac{c_H(p_{H_2}) - c_H(p_{H_2}^{ref})}{p_{H_2} - p_{H_2}^{ref}} \tag{5}$$

https://doi.org/10.1021/acsanm.2c01189
ACS Appl. Nano Mater. XXXX, XXX, XXX−XXX

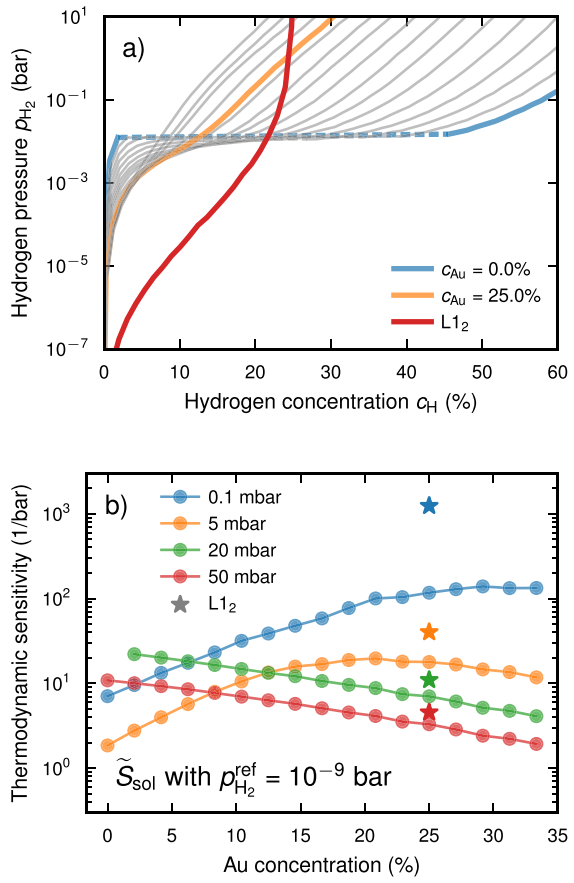

Figure 7. (a) Hydrogen partial pressure as a function of hydrogen concentration at a temperature of 300 K for different gold concentrations according to ref 25. The dashed lines indicate the miscibility gap between the H-poor α-phase and the H-rich β-phase. (b) Thermodynamic sensitivity $\tilde{S}_{sol}$ according to eq 5 using a reference pressure of $p^{ref}_{H_2} = 10^{-9}$ bar as a function of Au concentration at different H_2 partial pressures and a temperature of 300 K.

While there are some quantitative differences between these two measures, they show qualitatively the same behavior (Figure 7 and Figure S11).

The thermodynamic sensitivity varies with both Au concentration and H_2 partial pressure (Figure 7b). While at smaller partial pressures ($\lesssim$1 mbar) one obtains a monotonic *increase* of the thermodynamic sensitivity with Au content, at larger partial pressures ($\gtrsim$20 mbar) one actually observes a *decrease* of $\tilde{S}_{sol}$ with Au content. This behavior can be readily rationalized in terms of the pressure−concentration isotherms (Figure 7a). In the intermediate region around approximately 10 mbar, one observes a maximum, which shifts with hydrogen partial pressure.

Since the actual sensitivity S is simply the product of the optical sensitivity $\tilde{S}$ and the thermodynamic sensitivity S_{sol}, see eq 3, and the optical sensitivity does not strongly depend on Au concentration, the behavior described above should dominate the composition dependence of the actual sensitivity. One should, however, also take into account the fact that experiments are commonly carried out for ensembles of particles, for which the $p_{H_2}-c_H$ isotherms are considerably broadened. As a result, the variation of both the thermodynamic sensitivity (S_{sol} or $\tilde{S}_{sol}$) and the actual sensitivity (S) with Au concentration should be less pronounced than in the present case, which models the thermodynamic behavior of single particles under idealized conditions.

Detection Limit. Next, we translate our results to a detection limit in terms of hydrogen pressure. We assume a fixed optical sensitivity $\tilde{S}$ as defined by the gray, dashed line in Figure 5a (180 nm/(H/(Pd + Au))). We then explore the hydrogen pressure required to induce a certain LSPR peak shift (Figure 8a). In stable, experimental setups, a peak shift of 0.1

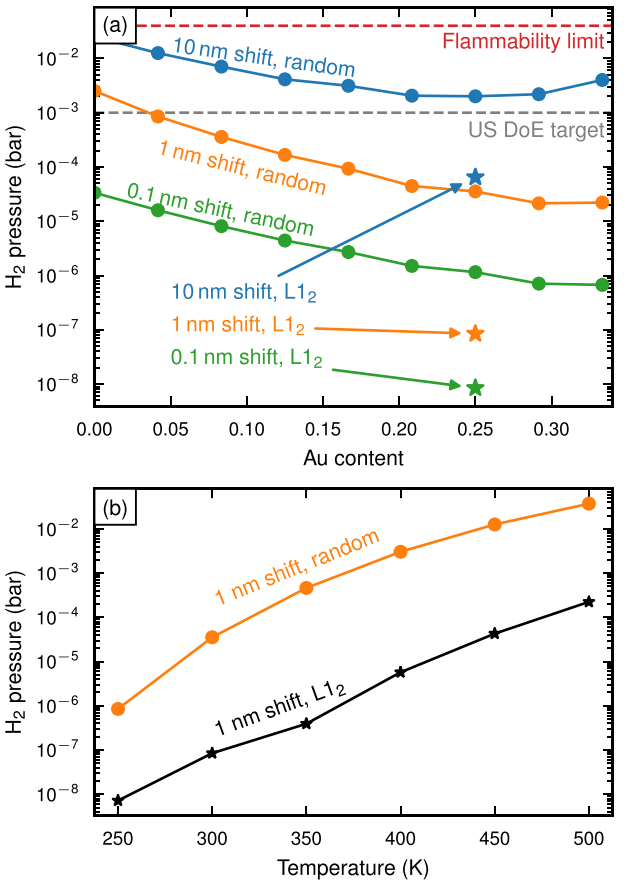

Figure 8. (a) Hydrogen pressure required to induce a peak shift of 10 nm (blue), 1 nm (orange), and 0.1 nm (green) at 300 K assuming a randomly ordered Pd−Au sublattice (dots) or $L1_2$ ordering (stars). Peaks shifts are calculated from the dashed, gray line in Figure 5a (180 nm/(H/(Au + Pd))) based on the relation between H_2 partial pressure and Au/H concentration calculated in ref 25. The flammability limit and the lower target for the detection limit of hydrogen sensors set by the US DoE[42] are marked in dashed red and gray, respectively. (b) Temperature dependence for the detection limit assuming a peak shift of 1 nm can be resolved for random $Pd_{0.75}Au_{0.25}$ (orange) and the same composition but with $L1_2$ ordering (black).

nm or less can be detected fairly easily. This implies that the detection limit is well below 1 mbar (green line in Figure 8a), which is approximately the target (1000 ppm) set by the U.S. Department of Energy (DOE) for hydrogen sensors[42] (dashed, gray line in Figure 8a). This is true regardless of Au content in the concentration interval studied here. Under more challenging circumstances, however, it cannot be ruled out that a more significant peak shift is required to obtain a reliable signal. With a 1 nm peak shift (orange line), nanodisks of pure

https://doi.org/10.1021/acsanm.2c01189
ACS Appl. Nano Mater. XXXX, XXX, XXX−XXX

Pd do not meet the U.S. DOE target, and at 10 nm (blue line), the target cannot be met at all.

Enhancing Sensitivity through Chemical Ordering. The situation can be substantially improved if we consider the ordered $L1_2$-Pd_3Au phase, which is expected to form when the alloy is subjected to high pressures of H_2.[25] This compound absorbs large amounts of hydrogen already at pressures below 10^{-5} bar, for which the regular alloy shows almost no sorption (Figure 7a), as observed in both experiments[26] and calculations[25] (also see Figure S10). As a result, one obtains a substantially larger thermodynamic sensitivity than for the regular alloy, especially for pressures of $\lesssim$1 mbar (stars in Figure 7b).

To evaluate the suitability of this $L1_2$-Pd_3Au compound for optical hydrogen detection, we calculated the dielectric function at different hydrogen contents and performed electrodynamic simulations in the same fashion as for the disordered phase (Figure S19). The results are very similar for the ordered and the disordered phase, with almost identically positioned LSPR peaks. We can thus assume the same sensitivity with respect to the peak position as for the disordered phase. The larger variation of the hydrogen uptake with pressure translates, however, to a detection limit that is predicted to be approximately 1−2 orders of magnitude lower in the ordered compound compared to the disordered phase, regardless of whether a large or small peak shift can be detected (stars in Figure 8a).

When temperature is increased, a higher hydrogen pressure is required to maintain the same hydrogen content in Pd−Au. Consequently, a higher hydrogen pressure is required to achieve a certain peak shift. The detection limit thus decreases with increasing temperature. The hydrogen uptake is, however, significantly higher in the $L1_2$-ordered phase than in the random phase, also at higher temperatures (Figure 8b). Hydrogen sensors based on the $L1_2$-ordered phase may thus retain a satisfactory detection limit at temperatures at which random alloys no longer meet the requirements.

CONCLUSIONS

Our results indicate that for all optical sensitivity measures, the disk diameter is the most relevant descriptor (Figure 5) in the selected span of geometries while disk height, AR, and alloy composition are of secondary importance. The highest optical sensitivities are found for larger particles, but for disk diameters above 150 nm the improvement is limited. For the optical sensitivity based on peak shift, our results reveal two separate regimes with respect to particle size (Figure 5a). For larger nanodisks ($d \gtrsim 100$ nm), the optical sensitivity is approximately constant at 180 nm/c_H. For smaller nanodisks ($d \lesssim 100$ nm), on the other hand, the optical sensitivity starts at a negative value and increases with decreasing particle size. This behavior originates from the emergence of a second peak that appears for H concentrations above 50%, caused by a localized interband transition, which becomes more apparent as the particle dimensions shrink.

The peak shift sensitivities obtained from electrodynamic simulations using the calculated DFs are comparable in magnitude to direct experimental measurements. They are, however, consistently larger and more importantly in the region where direct comparison is possible remain constant, whereas the experimental data show a linear shift with the absorption maximum. According to our calculations, while array effects and uncertainties in the particle size and shape distribution improve the agreement with experiment to some extent, the effect is too small to account for the deviation. To assess the contribution of the DFs, we also calculated the optical sensitivities using DFs from experiment. The results obtained using different experimentally measured DFs exhibit a spread that is comparable to the deviation between the optical sensitivities obtained using the calculated DFs and the direct measurements. This suggests that additional contributions to the DFs associated with scattering by, for example, defects are crucial. This highlights that the calculated DFs are in principle suitable for predictive simulations but that more work is required to assess more quantitatively the impact of sample-specific scattering and broadening channels.

Regardless, our simulations thus suggest that the optical sensitivity of individual nanoparticles cannot be significantly improved beyond the plateau that has been demonstrated here. For an array of nanoparticles, the optical sensitivity can, however, be improved by arranging them on a lattice and/or shifting the LSPR farther away from the avoided crossing, i.e., by increasing the nanodisk diameter far beyond 100 nm. In fact, the experimentally measured optical sensitivity in the far-infrared (i.e., for nanodisks with the largest diameters) clearly approaches the plateau value predicted here. Importantly, while from the experimental data one might anticipate the optical sensitivity to increase further for an even more extreme shift to the infrared (regardless of whether it is experimentally realizable or not), the present simulations provide strong evidence that there is an upper bound that is intrinsic for this kind of material and approach.

The actual sensitivity S comprises both the optical sensitivity $\tilde{S}$ and a thermodynamic factor S_{sol}, which depends on the solubility of hydrogen as a function of partial pressure. This thermodynamic sensitivity can vary rather strongly not only with the partial pressure of H_2 but the Au concentration. In particular for partial pressures near the α/β phase transition one can observe a strongly nonmonotonic variation with Au concentration with a maximum near the Au concentration at which the α/β two-phase region closes. While in experiments ensemble effects are likely to broaden this maximum, it remains a possible means to increase the actual sensitivity by alloying.

Another strategy to improve a H sensor is to increase the H uptake at a fixed hydrogen pressure, which means that for a specific optical sensitivity (measured optical shift per unit of absorbed H), lower hydrogen pressures can be detected. Here, we have shown that this can be achieved via an ordered $L1_2$-Pd_3Au phase, which can be obtained through annealing at high hydrogen pressures. Our simulations show that the optical response is largely unaffected by the presence of the ordered phase, which means that the optical sensitivity is unchanged. The H uptake, on the other hand, is significantly higher for the ordered phase which yields a detection limit 1−2 orders of magnitudes lower than for the disordered phase, well below the threshold stipulated by the U.S. Department of Energy (Figure 8). The possibilities provided by tuning the thermodynamic sensitivity through alloying demonstrated here have potentially notable implications for the field of plasmonic H sensing.

METHOD SECTION

Calculation of Dielectric Functions. SQSs[27] were generated with the ICET package[43] using the method and parameters suggested in ref 44. The ionic positions and cell

https://doi.org/10.1021/acsanm.2c01189
ACS Appl. Nano Mater. XXXX, XXX, XXX−XXX

shapes of these structures were relaxed with density-functional theory (DFT) in the projector augmented wave formalism as implemented in the Vienna ab initio simulation package (version 5.4.1, PAW 2015)[45,46] using the vdW-DF-cx exchange−correlation functional,[47] until residual forces were below 10 meV/Å and stresses below 1 kbar. In these calculations, the wave functions were expanded in a plane wave basis set with a cutoff of 384 eV, and the Brillouin zone was sampled with a Γ-centered grid with a k-point density corresponding to 19 × 19 × 19 k-points in the primitive cell. Occupations were set using the first-order Methfessel−Paxton scheme with a smearing parameter of 0.1 eV.

DFs were calculated using random phase approximation (RPA)−linear-response time-dependent density-functional theory as implemented in the GPAW package[48,49] (version 19.8.1 with GLLB-sc patched for extended metallic systems). The macroscopic DF was calculated in reciprocal space through the linear density−density response function with wave functions expanded in a plane-wave basis with a cutoff at 350 eV. The BZ was sampled with a Γ-centered grid with a density corresponding to 61 k-points in each direction for the undecorated (monoelemental) primitive cell, and occupation numbers were smeared using a Fermi−Dirac distribution with a width of 0.1 eV.

DFs were obtained in the optical limit by evaluation at $q = 0$. As discrete k-point sampling precludes intraband transitions with $q \to 0$ and $\omega \to 0$, an intraband term, $\omega_P^2/(\omega + i\eta)^2$, was added to the DFs, where ω_P is the calculated plasma frequency, using the broadening parameter $\eta = 0.01$ eV. The ground state wave functions were obtained with the GLLB-sc exchange−correlation functional,[50] whereas dynamic exchange−correlation effects were neglected; i.e., the RPA approximation was used. In the optical limit, adiabatic local-density approximation (ALDA) results approach the RPA results, meaning virtually identical results would have been obtained if dynamic exchange−correlation effects had been taken into account using ALDA.

Finite-Difference Time-Domain Simulations. Single particle extinction spectra were calculated using finite-difference time-domain simulations as implemented in the MEEP software.[51] The computational cell consists of a $Pd_{1-y}Au_yH_x$ nanodisk (represented by the calculated DFs fitted to a Lorentzian representation as described in Supplementary Note 1; refs 52−54) placed on a 100 nm thick SiO_2 substrate with constant refractive index 1.478. The nanodisk has truncated-cone geometry with fixed cone angle $\theta = 60°$, varying (bottom) diameter d and height h (Figure 2a). To account for the expansion that occurs with H absorption in a real system, the system size is scaled with H content according to the lattice parameter expansion obtained from the DFT calculations. The source is a Gaussian pulse at normal incidence corresponding to the energy interval 1−5 eV. To mimic an infinite system, a 100 nm thick perfectly matched layer encloses the cell at a distance of at least 100 nm from the nanodisk in all directions, to enable a sufficiently large vacuum region. The cell is described in Cartesian coordinates with a grid resolution of 0.5 pixels/nm.

A detailed description of the procedure of calculating extinction spectra can be found in Supplementary Note 2. In the data analysis, a peak in the extinction spectrum is defined as a point in the extinction spectra with larger amplitude than the two neighboring points. For the peak shift sensitivity calculation, only peaks with higher amplitude than the mean over the entire spectrum were included. Calculating the sensitivity involves a linear fit of the studied shift with H content. In this work, we employ Huber regression as implemented in SCIKIT-LEARN[55] for this purpose.

T-Matrix Simulations. Nanodisk array extinction spectra were calculated using a T-matrix based approach as implemented in SMUTHI.[56] The method allows for calculating the response of a substrate-supported single disk of varying geometry, as well as large arrays composed of hundreds of such particles. Note that for the nanodisk arrays, cylindrical disks where simulated instead of truncated cones, which has a negligible effect on the resulting extinction spectra (Figure S5). Arrays were treated either as amorphous and described statistically by the pair correlation function dependent on a minimum center-to-center distance between disks (as previously demonstrated[57,58]) or as arrays consisting of 100 randomly distributed resonators with explicitly defined positions (see Figure S16b). For the latter case, size distribution within the array is also taken into account.

■ ASSOCIATED CONTENT

Supporting Information

The Supporting Information is available free of charge at https://pubs.acs.org/doi/10.1021/acsanm.2c01189.

Additional visualizations of the DOS and DFs, nanodisk shape effects on the extinction spectrum, additional visualizations of extinction spectra, extended analysis of the double peak phenomenon of PdH, near-field enhancement obtained from electrodynamic simulations, hydrogen uptake as a function of the pressure and alloy composition, extended analysis of the peak shift sensitivity, effect of artificial broadening on the extinction spectra and the resulting sensitivity, particle size distribution and array effects on the optical response, optical response of the $L1_2$-ordered phase, and visual representation of the DF fitting procedure (PDF)

■ AUTHOR INFORMATION

Corresponding Author

Paul Erhart − *Department of Physics, Chalmers University of Technology, SE-412 96 Gothenburg, Sweden;* orcid.org/0000-0002-2516-6061; Email: erhart@chalmers.se

Authors

Pernilla Ekborg-Tanner − *Department of Physics, Chalmers University of Technology, SE-412 96 Gothenburg, Sweden;* orcid.org/0000-0002-9427-4816

J. Magnus Rahm − *Department of Physics, Chalmers University of Technology, SE-412 96 Gothenburg, Sweden;* orcid.org/0000-0002-6777-0371

Victor Rosendal − *Department of Physics, Chalmers University of Technology, SE-412 96 Gothenburg, Sweden*

Maria Bancerek − *Faculty of Physics, University of Warsaw, PL-02-093 Warsaw, Poland; Department of Physics, Chalmers University of Technology, SE-412 96 Gothenburg, Sweden*

Tuomas P. Rossi − *Department of Applied Physics, Aalto University, FI-00076 Aalto, Finland;* orcid.org/0000-0002-8713-4559

Tomasz J. Antosiewicz − *Faculty of Physics, University of Warsaw, PL-02-093 Warsaw, Poland; Department of*

https://doi.org/10.1021/acsanm.2c01189
ACS Appl. Nano Mater. XXXX, XXX, XXX−XXX

Physics, Chalmers University of Technology, SE-412 96 Gothenburg, Sweden; orcid.org/0000-0003-2535-4174

Complete contact information is available at: https://pubs.acs.org/10.1021/acsanm.2c01189

Notes

The authors declare no competing financial interest.

The raw dielectric functions are provided via Zenodo at https://doi.org/10.5281/zenodo.5833929.

■ ACKNOWLEDGMENTS

This work was funded by the Knut and Alice Wallenberg Foundation (Grants 2015.0055 and 2019.0140), the Swedish Foundation for Strategic Research Materials framework (Grant RMA15-0052), the Swedish National Research Council (Grants 2018-06482 and 2020-04935), and the Excellence Initiative Nano at Chalmers. T.P.R. acknowledges funding from Academy of Finland under Grant Agreement 332429. T.J.A. acknowledges support from the National Science Center, Poland, via Project 2019/35/B/ST5/02477. The computations were enabled by resources provided by the Swedish National Infrastructure for Computing (SNIC) at NSC, C3SE, and PDC partially funded by the Swedish Research Council through Grant Agreement 2018-05973 and the Interdisciplinary Center for Mathematical and Computational Modelling via Project GC84-51.

■ REFERENCES

(1) Dutta, S. A Review on Production, Storage of Hydrogen and Its Utilization As an Energy Resource. *J. Ind. Eng. Chem.* **2014**, *20*, 1148−1156.

(2) Langhammer, C.; Zorić, I.; Kasemo, B.; Clemens, B. M. Hydrogen Storage in Pd Nanodisks Characterized with a Novel Nanoplasmonic Sensing Scheme. *Nano Lett.* **2007**, *7*, 3122−3127.

(3) Langhammer, C.; Larsson, E. M.; Kasemo, B.; Zorić, I. Indirect Nanoplasmonic Sensing: Ultrasensitive Experimental Platform for Nanomaterials Science and Optical Nanocalorimetry. *Nano Lett.* **2010**, *10*, 3529−3538.

(4) Liu, N.; Tang, M. L.; Hentschel, M.; Giessen, H.; Alivisatos, A. P. Nanoantenna-Enhanced Gas Sensing in a Single Tailored Nanofocus. *Nat. Mater.* **2011**, *10*, 631−636.

(5) Boelsma, C.; Bannenberg, L. J.; van Setten, M. J.; Steinke, N.-J.; van Well, A. A.; Dam, B. Hafnium—An Optical Hydrogen Sensor Spanning Six Orders in Pressure. *Nat. Commun.* **2017**, *8*, 15718.

(6) Nugroho, F. A. A.; Darmadi, I.; Zhdanov, V. P.; Langhammer, C. Universal Scaling and Design Rules of Hydrogen-Induced Optical Properties in Pd and Pd-Alloy Nanoparticles. *ACS Nano* **2018**, *12*, 9903−9912.

(7) She, X.; Shen, Y.; Wang, J.; Jin, C. Pd Films on Soft Substrates: A Visual, High-Contrast and Low-Cost Optical Hydrogen Sensor. *Light Sci. Appl.* **2019**, *8*, 4.

(8) Beni, T.; Yamasaku, N.; Kurotsu, T.; To, N.; Okazaki, S.; Arakawa, T.; Balčytis, A.; Seniutinas, G.; Juodkazis, S.; Nishijima, Y. Metamaterial for Hydrogen Sensing. *ACS Sens* **2019**, *4*, 2389−2394.

(9) Nugroho, F. A. A.; Darmadi, I.; Cusinato, L.; Susarrey-Arce, A.; Schreuders, H.; Bannenberg, L. J.; Bastos da Silva Fanta, A.; Kadkhodazadeh, S.; Wagner, J. B.; Antosiewicz, T. J.; Hellman, A.; Zhdanov, V. P.; Dam, B.; Langhammer, C. Metal−Polymer Hybrid Nanomaterials for Plasmonic Ultrafast Hydrogen Detection. *Nat. Mater.* **2019**, *18*, 489−495.

(10) Sterl, F.; Strohfeldt, N.; Both, S.; Herkert, E.; Weiss, T.; Giessen, H. Design Principles for Sensitivity Optimization in Plasmonic Hydrogen Sensors. *ACS Sens* **2020**, *5*, 917−927.

(11) Bannenberg, L.; Schreuders, H.; Dam, B. Tantalum-Palladium: Hysteresis-Free Optical Hydrogen Sensor Over 7 Orders of Magnitude in Pressure with Sub-Second Response. *Adv. Funct. Mater.* **2021**, *31*, 2010483.

(12) Losurdo, M.; Gutiérrez, Y.; Suvorova, A.; Giangregorio, M. M.; Rubanov, S.; Brown, A. S.; Moreno, F. Gallium Plasmonic Nanoantennas Unveiling Multiple Kinetics of Hydrogen Sensing, Storage, and Spillover. *Adv. Mater.* **2021**, *33*, 2100500.

(13) Hassan, K.; Iftekhar Uddin, A. S. M.; Chung, G.-S. Fast-Response Hydrogen Sensors Based on Discrete Pt/Pd Bimetallic Ultra-Thin Films. *Sens. Actuators, B* **2016**, *234*, 435−445.

(14) Kabcum, S.; Channei, D.; Tuantranont, A.; Wisitsoraat, A.; Liewhiran, C.; Phanichphant, S. Ultra-Responsive Hydrogen Gas Sensors Based on PdO Nanoparticle-Decorated WO_3 Nanorods Synthesized by Precipitation and Impregnation Methods. *Sens. Actuators, B* **2016**, *226*, 76−89.

(15) Alenezy, E. K.; Sabri, Y. M.; Kandjani, A. E.; Korcoban, D.; Abdul Haroon Rashid, S. S. A.; Ippolito, S. J.; Bhargava, S. K. Low-Temperature Hydrogen Sensor: Enhanced Performance Enabled through Photoactive Pd-Decorated TiO_2 Colloidal Crystals. *ACS Sens* **2020**, *5*, 3902−3914.

(16) Griessen, R.; Strohfeldt, N.; Giessen, H. Thermodynamics of the Hybrid Interaction of Hydrogen with Palladium Nanoparticles. *Nat. Mater.* **2016**, *15*, 311−317.

(17) Wadell, C.; Nugroho, F. A. A.; Lidström, E.; Iandolo, B.; Wagner, J. B.; Langhammer, C. Hysteresis-Free Nanoplasmonic Pd−Au Alloy Hydrogen Sensors. *Nano Lett.* **2015**, *15*, 3563−3570.

(18) Darmadi, I.; Nugroho, F. A. A.; Langhammer, C. High-Performance Nanostructured Palladium-Based Hydrogen Sensors—Current Limitations and Strategies for Their Mitigation. *ACS Sens* **2020**, *5*, 3306−3327.

(19) Maeland, A.; Flanagan, T. B. X-Ray and Thermodynamic Studies of the Absorption of Hydrogen by Gold-Palladium Alloys. *J. Phys. Chem.* **1965**, *69*, 3575−3581.

(20) Westerwaal, R. J.; Rooijmans, J. S. A.; Leclercq, L.; Gheorghe, D. G.; Radeva, T.; Mooij, L.; Mak, T.; Polak, L.; Slaman, M.; Dam, B.; Rasing, T. Nanostructured Pd−Au Based Fiber Optic Sensors for Probing Hydrogen Concentrations in Gas Mixtures. *Int. J. Hydrogen Energy* **2013**, *38*, 4201−4212.

(21) Darmadi, I.; Khairunnisa, S. Z.; Tomeček, D.; Langhammer, C. Optimization of the Composition of PdAuCu Ternary Alloy Nanoparticles for Plasmonic Hydrogen Sensing. *ACS Appl. Nano Mater.* **2021**, *4*, 8716−8722.

(22) Rahm, J. M.; Tiburski, C.; Rossi, T. P.; Nugroho, F. A. A.; Nilsson, S.; Langhammer, C.; Erhart, P. A Library of Late Transition Metal Alloy Dielectric Functions for Nanophotonic Applications. *Adv. Funct. Mater.* **2020**, *30*, 2002122.

(23) Poyli, M. A.; Silkin, V. M.; Chernov, I. P.; Echenique, P. M.; Muiño, R. D.; Aizpurua, J. Multiscale Theoretical Modeling of Plasmonic Sensing of Hydrogen Uptake in Palladium Nanodisks. *J. Phys. Chem. Lett.* **2012**, *3*, 2556−2561.

(24) Silkin, V. M.; Muiño, R. D.; Chernov, I. P.; Chulkov, E. V.; Echenique, P. M. Tuning the Plasmon Energy of Palladium−Hydrogen Systems by Varying the Hydrogen Concentration. *J. Phys.: Condens. Matter* **2012**, *24*, 104021.

(25) Rahm, J. M.; Löfgren, J.; Fransson, E.; Erhart, P. A Tale of Two Phase Diagrams: Interplay of Ordering and Hydrogen Uptake in Pd−Au−H. *Acta Mater.* **2021**, *211*, 116893.

(26) Lee, S.-M.; Noh, H.; Flanagan, T. B.; Luo, S. Hydrogen-Induced Lattice Rearrangement of a $Pd_{0.81}Au_{0.19}$ Alloy. *J. Phys.: Condens. Matter* **2007**, *19*, 326222.

(27) Zunger, A.; Wei, S. H.; Ferreira, L. G.; Bernard, J. E. Special Quasirandom Structures. *Phys. Rev. Lett.* **1990**, *65*, 353−356.

(28) Chandrasekhar, N.; Sholl, D. S. Computational Study of Hydrogen Induced Lattice Rearrangement and Its Influence on Hydrogen Permeance in Pd−Au Alloys. *J. Alloys Compd.* **2014**, *609*, 244−252.

(29) Palm, K. J.; Murray, J. B.; Narayan, T. C.; Munday, J. N. Dynamic Optical Properties of Metal Hydrides. *ACS Photonics* **2018**, *5*, 4677−4686.

(30) Vargas, W. E.; Azofeifa, D. E.; Clark, N.; Solis, H.; Montealegre, F.; Cambronero, M. Parametric formulation of the dielectric function of palladium and palladium hydride thin films. *Appl. Opt.* **2014**, *53*, 5294−5306.
(31) It is only at higher Au content that the distance between the d band and the Fermi level becomes significant.[22,59]
(32) Fredriksson, H.; Alaverdyan, Y.; Dmitriev, A.; Langhammer, C.; Sutherland, D. S.; Zäch, M.; Kasemo, B. Hole−Mask Colloidal Lithography. *Adv. Mater.* **2007**, *19*, 4297−4302.
(33) Pakizeh, T. Optical Absorption of Plasmonic Nanoparticles in Presence of a Local Interband Transition. *J. Phys. Chem. C* **2011**, *115*, 21826−21831.
(34) Pirzadeh, Z.; Pakizeh, T.; Miljkovic, V.; Langhammer, C.; Dmitriev, A. Plasmon−Interband Coupling in Nickel Nanoantennas. *ACS Photonics* **2014**, *1*, 158−162.
(35) In the sensitivity analysis, we exclude all peaks below the mean extinction over the spectrum since those are in practice not of importance.
(36) Here, the experimental peak position at 0% H has been converted to disk diameter based on our obtained linear relationship (Figure S12b) and the sensitivity is rescaled from H concentration with respect to Pd to the total H concentration. An equivalent comparison based on peak position at 0% H can be found in Figure S12a.
(37) The definition of the onset is arbitrary and does not have to be based on the peak. Here we use 50% of the peak amplitude as a convenient measure when comparing sensitivity over the span of geometries.
(38) The exact concentration of the hydride is 67% for the Silkin et al. DF, 62% for the Palm et al. DF, and 58% for the Vargas et al. DF due to the concentrations of the available data.
(39) Antosiewicz, T. J.; Tarkowski, T. Localized Surface Plasmon Decay Pathways in Disordered Two-Dimensional Nanoparticle Arrays. *ACS Photonics* **2015**, *2*, 1732−1738.
(40) Czajkowski, K. M.; Antosiewicz, T. J. Effective dipolar polarizability of amorphous arrays of size-dispersed nanoparticles. *Opt. Lett.* **2020**, *45*, 3220−3223.
(41) Villegas, C. E. P.; Leite, M. S.; Marini, A.; Rocha, A. R. Efficient hot-carrier dynamics in near-infrared photocatalytic metals. *Phys. Rev. B* **2022**, *105*, 165109.
(42) Multi-Year Research, Development, and Demonstration Plan, 2011−2020: Section 3.7 Hydrogen Safety, Codes and Standards. U.S. Department of Energy, Energy Efficiency and Renewable Energy (EERE), Fuel Cell Technologies Office, 2015.
(43) Ångqvist, M.; Muñoz, W. A.; Rahm, J. M.; Fransson, E.; Durniak, C.; Rozyczko, P.; Rod, T. H.; Erhart, P. ICET − A Python Library for Constructing and Sampling Alloy Cluster Expansions. *Adv. Theor. Simul.* **2019**, *2*, 1900015.
(44) Van De Walle, A.; Tiwary, P.; De Jong, M.; Olmsted, D. L.; Asta, M.; Dick, A.; Shin, D.; Wang, Y.; Chen, L. Q.; Liu, Z. K. Efficient Stochastic Generation of Special Quasirandom Structures. *CALPHAD: Comput. Coupling Phase Diagrams Thermochem.* **2013**, *42*, 13−18.
(45) Kresse, G.; Furthmüller, J. Efficiency of Ab-Initio Total Energy Calculations for Metals and Semiconductors Using a Plane-Wave Basis Set. *Comput. Mater. Sci.* **1996**, *6*, 15−50.
(46) Kresse, G.; Joubert, D. From Ultrasoft Pseudopotentials to the Projector Augmented-Wave Method. *Phys. Rev. B* **1999**, *59*, 1758−1775.
(47) Berland, K.; Hyldgaard, P. Exchange Functional that Tests the Robustness of the Plasmon Description of the Van der Waals Density Functional. *Phys. Rev. B* **2014**, *89*, 035412.
(48) Enkovaara, J.; Rostgaard, C.; Mortensen, J. J.; Chen, J.; Dułak, M.; Ferrighi, L.; Gavnholt, J.; Glinsvad, C.; Haikola, V.; Hansen, H. A.; Kristoffersen, H. H.; Kuisma, M.; Larsen, A. H.; Lehtovaara, L.; Ljungberg, M.; Lopez-Acevedo, O.; Moses, P. G.; Ojanen, J.; Olsen, T.; Petzold, V.; Romero, N. A.; Stausholm-Møller, J.; Strange, M.; Tritsaris, G. A.; Vanin, M.; Walter, M.; Hammer, B.; Häkkinen, H.; Madsen, G. K. H.; Nieminen, R. M.; Nørskov, J. K.; Puska, M.; Rantala, T. T.; Schiøtz, J.; Thygesen, K. S.; Jacobsen, K. W. Electronic Structure Calculations with GPAW: A Real-Space Implementation of the Projector Augmented-Wave Method. *J. Phys.: Condens. Matter* **2010**, *22*, 253202.
(49) Yan, J.; Mortensen, J. J.; Jacobsen, K. W.; Thygesen, K. S. Linear Density Response Function in the Projector Augmented Wave Method: Applications to Solids, Surfaces, and Interfaces. *Phys. Rev. B* **2011**, *83*, 245122.
(50) Kuisma, M.; Ojanen, J.; Enkovaara, J.; Rantala, T. T. Kohn-Sham Potential with Discontinuity for Band Gap Materials. *Phys. Rev. B* **2010**, *82*, 115106.
(51) Oskooi, A. F.; Roundy, D.; Ibanescu, M.; Bermel, P.; Joannopoulos, J.; Johnson, S. G. Meep: A Flexible Free-Software Package for Electromagnetic Simulations by the FDTD Method. *Comput. Phys. Commun.* **2010**, *181*, 687−702.
(52) Eriksson, F.; Fransson, E.; Erhart, P. The Hiphive Package for the Extraction of High-Order Force Constants by Machine Learning. *Adv. Theor. Simul.* **2019**, *2*, 1800184.
(53) Schwarz, G. Estimating the Dimension of a Model. *Ann. Statist.* **1978**, *6*, 461−464.
(54) Virtanen, P.; Gommers, R.; Oliphant, T. E.; Haberland, M.; Reddy, T.; Cournapeau, D.; Burovski, E.; Peterson, P.; Weckesser, W.; Bright, J.; van der Walt, S. J.; Brett, M.; Wilson, J.; Millman, K. J.; Mayorov, N.; Nelson, A. R. J.; Jones, E.; Kern, R.; Larson, E.; Carey, C. J.; Polat, İ.; Feng, Y.; Moore, E. W.; VanderPlas, J.; Laxalde, D.; Perktold, J.; Cimrman, R.; Henriksen, I.; Quintero, E. A.; Harris, C. R.; Archibald, A. M.; Ribeiro, A. H.; Pedregosa, F.; van Mulbregt, P.; SciPy 1.0 Contributors.. SciPy 1.0: Fundamental Algorithms for Scientific Computing in Python. *Nat. Methods* **2020**, *17*, 261−272.
(55) Pedregosa, F.; Varoquaux, G.; Gramfort, A.; Michel, V.; Thirion, B.; Grisel, O.; Blondel, M.; Prettenhofer, P.; Weiss, R.; Dubourg, V.; Vanderplas, J.; Passos, A.; Cournapeau, D.; Brucher, M.; Perrot, M.; Duchesnay, E. Scikit-learn: Machine Learning in Python. *J. Mach. Learn. Res.* **2011**, *12*, 2825−2830.
(56) Egel, A.; Czajkowski, K. M.; Theobald, D.; Ladutenko, K.; Kuznetsov, A. S.; Pattelli, L. SMUTHI: A python package for the simulation of light scattering by multiple particles near or between planar interfaces. *Journal of Quantitative Spectroscopy and Radiative Transfer* **2021**, *273*, 107846.
(57) Antosiewicz, T. J.; Apell, S. P.; Zäch, M.; Zorić, I.; Langhammer, C. Oscillatory Optical Response of an Amorphous Two-Dimensional Array of Gold Nanoparticles. *Phys. Rev. Lett.* **2012**, *109*, 247401.
(58) Czajkowski, K. M.; Bancerek, M.; Antosiewicz, T. J. Multipole analysis of substrate-supported dielectric nanoresonator metasurfaces via the *T*-matrix method. *Phys. Rev. B* **2020**, *102*, 085431.
(59) Nahm, T.-U.; Jung, R.; Kim, J.-Y.; Park, W.-G.; Oh, S.-J.; Park, J.-H.; Allen, J. W.; Chung, S.-M.; Lee, Y. S.; Whang, C. N. Electronic Structure of Disordered Au−Pd Alloys Studied by Electron Spectroscopies. *Phys. Rev. B* **1998**, *58*, 9817−9825.

https://doi.org/10.1021/acsanm.2c01189
ACS Appl. Nano Mater. XXXX, XXX, XXX−XXX